AIAA 99-0231

Simulation of Acoustic Scattering from a Trailing Edge

Bart A. Singer, Kenneth S. Brentner,
David P. Lockard
NASA Langley Research Center
Hampton, VA 23681-2199

Geoffrey M. Lilley
ICASE
NASA Langley Research Center
Hampton, VA 23681-2199

37th Aerospace Sciences Meeting & Exhibit
January 11-14, 1999, Reno, NV

SIMULATION OF ACOUSTIC SCATTERING FROM A TRAILING EDGE

Bart A. Singer*, Kenneth S. Brentner†,
David P. Lockard‡
NASA Langley Research Center
Hampton, VA 23681-2199

Geoffrey M. Lilley§
ICASE
NASA Langley Research Center
Hampton, VA 23681-2199

Three model problems were examined to assess the difficulties involved in using a hybrid scheme coupling flow computation with the the Ffowcs Williams and Hawkings equation to predict noise generated by vortices passing over a sharp edge. The results indicate that the Ffowcs Williams and Hawkings equation correctly propagates the acoustic signals when provided with accurate flow information on the integration surface. The most difficult of the model problems investigated inviscid flow over a two-dimensional thin NACA airfoil with a bluff-body vortex generator positioned at 98 percent chord. Vortices rolled up downstream of the bluff body. The shed vortices possessed similarities to large coherent eddies in boundary layers. They interacted and occasionally paired as they convected past the sharp trailing edge of the airfoil. The calculations showed acoustic waves emanating from the airfoil trailing edge. Acoustic directivity and Mach number scaling are shown.

Introduction

In the theory of aerodynamic noise developed by Lighthill[1,2] turbulent fluctuations in free space are particularly inefficient radiators of noise in a low-speed flow. The turbulent fluctuations are quadrupole-type sources and hence the radiated acoustic intensity varies as a characteristic velocity scale u to the eighth power. However, when a turbulent eddy passes in the vicinity of a sharp edge of a solid surface, the character of the far-field acoustic radiation changes dramatically and the turbulent fluctuations radiate much more strongly.

Ffowcs Williams and Hall[3] first investigated this problem by modeling a typical turbulent eddy as a quadrupole point source near the edge of a half plane. They found the controlling parameter to be kr_0 where k is the acoustic wavenumber ω/c, ω is the radian acoustic frequency, c is the speed of sound, and r_0 is the distance from the quadrupole to the edge of the half plane. For quadrupoles having fluid motion in a plane perpendicular to the edge, and for which $2kr_0 << 1$, the sound output from the associated quadrupoles increases by a factor of $(kr_0)^{-3}$. With the additional assumptions that the eddy perturbation velocity and the acoustic frequency scale linearly with the characteristic velocity scale u, Ffowcs Williams and Hall[3] found that the acoustic intensity increases by a factor of u^{-3} relative to the case of quadrupoles in free space. This means that a quadrupole noise source in the vicinity of a sharp edge radiates noise proportional to u^5, which for low-Mach-number flows is greater than the u^6 scaling in the case of Curle's[4] surface dipoles for acoustically compact surfaces. Ffowcs Williams and Hall[3] also found that the intensity varies as $\sin^2(\theta/2)$, where θ is the angle measured relative to the downstream extension of the plate. Subsequent analysis by Goldstein[5] confirmed the findings of Ffowcs Williams and Hall.[3]

Crighton[6] calculated the acoustic field generated by a line vortex passing around the edge of a rigid half plane by matching the complex potential flow solution with a slightly compressible solution. His results show that the presence of the edge increases

*Research Scientist, Aerodynamic and Acoustic Methods Branch.

†Senior Research Engineer, Aerodynamic and Acoustic Methods Branch, Senior Member AIAA.

‡Research Scientist, Aerodynamic and Acoustic Methods Branch, Member AIAA.

§Chief Scientist, Senior Member AIAA.

the acoustic energy radiated by the vortex by an amount proportional to M^{-3}, where $M \equiv u/c$ is a characteristic Mach number for the flow. This result is consistent with all scattering theories at low Mach number.

Howe[7] reviewed various trailing-edge theories and showed that for low-Mach-number flow they all give essentially the same predictions when properly interpreted. Howe then extended the theory of trailing-edge noise to include the effects of source motion relative to the trailing edge, Doppler-shift, and whether or not an unsteady Kutta condition is applied at the trailing edge. None of his extensions alter the important scaling relations obtained in the original analysis of Ffowcs-Williams and Hall.[3]

The theoretical predictions were largely supported by the results of the Brooks and Hodgson[8] trailing-edge noise experiments on a NACA0012 airfoil at low incidence in an anechoic quiet-flow facility. They mounted surface-pressure sensors near the airfoil trailing edge to obtain unsteady surface-pressure data and measured the radiated noise with microphones placed at various angular positions between two and four chord lengths away from the trailing edge. Among other findings, their results confirmed that the acoustic signal scattered from a turbulent boundary layer on an airfoil with a sharp trailing edge scales with u^5 and the directivity was proportional to $\sin^2(\theta/2)$.

Calculation methods for acoustic fields comprised of trailing-edge noise currently are largely empirical.[9] In this work we explore the feasibility of directly computing the acoustic field generated by flow over a sharp trailing edge. A hybrid computational approach is taken wherein a commonly used, general purpose computational fluid dynamics (CFD) solver is used to accurately calculate the unsteady fluid dynamics over a relatively small region near the surface, and an acoustics code based on the Ffowcs Williams and Hawkings[10] (FW–H) equation computes the acoustic field generated by the previously calculated unsteady near flow field.

As a first step in this feasibility analysis, the flow around a circular cylinder with unsteady vortex shedding is analyzed. Although the noise produced by unsteady vortex shedding is different than that produced by sharp trailing edges, both flows involve the formation of wakes. Prior uses of codes based on the FW–H equation have not investigated the situation where a permeable integration surface cuts through the wake. We demonstrate that the FW–H equation, rather than the Kirchoff formulation, is appropriate for this condition.

Following successful resolution of the wake issue, the numerical solution of the FW–H equation is compared to the exact analytic solution found by Crighton for a line vortex traveling around the edge of a flat plate. This test problem confirms the ability of the FW–H acoustics code to correctly propagate acoustic signals arising from scattering processes.

Finally, a model problem involving vortices convecting past the sharp trailing edge of an airfoil is investigated. The vortices approximate large-scale flow structures present in turbulent flows. The unsteady flow field from the CFD calculation is used as input for the FW–H acoustics code. Noise spectra, directivity, and Mach number scaling are obtained without the introduction of empirical constants.

Computational Tools

CFL3D

The computer code, CFL3D[11,12] is used to compute the unsteady flow field. CFL3D was developed at NASA Langley Research Center to solve the three-dimensional, time-dependent, thin-layer (in each coordinate direction) Reynolds-averaged Navier-Stokes (RANS) equations using a finite-volume formulation. The code uses upwind-biased spatial differencing for the inviscid terms and flux-limiting to obtain smooth solutions in the vicinity of shock waves. The viscous derivatives, when used, are computed by second-order central differencing. Fluxes at the cell faces are calculated by the flux-difference-splitting method of Roe.[13] An implicit three-factor approximate factorization method is used to advance the solution in time. Patched grid interfaces, implemented by Biedron and Thomas,[14] are used at several of the zone boundaries to reduce the total number of grid points in the calculation.

The time-dependent version of CFL3D uses subiterations to obtain second order temporal accuracy. The $\tau - TS$ subiteration option[15] is exercised in this work. In this option, each of the sub-iterations is advanced with a pseudo-time step. This approach facilitates a more rapid convergence to the result at each physical time step. In our calculations, four sub-iterations are used for each physical time step.

Although the low-order numerical techniques used in CFL3D are a possible source of concern in acoustic applications, recently Rumsey, Biedron, Farassat and Spence[16] successfully used CFL3D to compute the generation and near-field propagation of acoustic modes through a ducted-fan engine. Their work demonstrated that CFL3D can calculate the unsteady compressible flow, including the acoustics, when appropriate grids and time steps are used.

Ffowcs Williams and Hawkings Code

The Ffowcs Williams and Hawkings[10] equation is the most general form of the Lighthill acoustic analogy and is appropriate for computing the acoustic field generated by an accurate, unsteady flow calculation. Following Brentner and Farassat,[17] the FW–H equation may be written in differential form as

$$\Box^2 p'(\mathbf{x},t) = \frac{\partial^2}{\partial x_i \partial x_j}[T_{ij}H(f)] - \frac{\partial}{\partial x_i}[L_i\delta(f)] + \frac{\partial}{\partial t}[(\rho_0 U_n)\delta(f)] \quad (1)$$

where: $\Box^2 \equiv \frac{1}{c^2}\frac{\partial^2}{\partial t^2} - \nabla^2$ is the wave operator, c is the speed of ambient sound, t is observer time, $p' \equiv \rho' c^2$ (on the left-hand side) is the acoustic pressure, ρ' is the perturbation density, ρ_0 is the free-stream density, $f = 0$ describes the integration surface, $\delta(f)$ is the Dirac delta function, and $H(f)$ is the Heaviside function. The quantities U_i and L_i are defined as

$$U_i = (1 - \frac{\rho}{\rho_0})v_i + \frac{\rho u_i}{\rho_0} \quad (2)$$

and

$$L_i = P_{ij}\hat{n}_j + \rho u_i(u_n - v_n) \quad (3)$$

respectively. In the above equations, ρ is the total density, ρu_i, is the momentum in the i direction, v_i is the velocity of the integration surface $f = 0$, and P_{ij} is the compressive stress tensor. For an inviscid fluid, $P_{ij} = p'\delta_{ij}$ where δ_{ij} is the Kronecker delta. The subscript n indicates the projection of a vector quantity in the surface normal direction.

An integral representation of the solution to Eq. (1) can be written directly by utilizing formulation 1A of Farassat,[18,19] which is written

$$p'(\mathbf{x},t) = p'_T(\mathbf{x},t) + p'_L(\mathbf{x},t) + p'_Q(\mathbf{x},t) \quad (4)$$

where

$$4\pi p'_T(\mathbf{x},t) = \int_{f=0} \Big[\frac{\rho_0(\dot{U}_n + U_{\dot{n}})}{r(1-M_r)^2}\Big]_{ret} dS + \int_{f=0} \Big[\frac{\rho_0 U_n(r\dot{M}_r + c(M_r - M^2))}{r^2(1-M_r)^3}\Big]_{ret} dS \quad (5)$$

$$4\pi p'_L(\mathbf{x},t) = \frac{1}{c}\int_{f=0} \Big[\frac{\dot{L}_r}{r(1-M_r)^2}\Big]_{ret} dS + \int_{f=0} \Big[\frac{L_r - L_M}{r^2(1-M_r)^2}\Big]_{ret} dS + \frac{1}{c}\int_{f=0} \Big[\frac{L_r(r\dot{M}_r + c(M_r - M^2))}{r^2(1-M_r)^3}\Big]_{ret} dS \quad (6)$$

Here the dot indicates a time derivative, $L_M = L_i M_i$ where M_i is the Mach number in the i^{th} coordinate direction, r is the distance from a source point on the surface to the observer, and the subscript r indicates the projection of a vector quantity in the radiation direction. The quadrupole term $p'_Q(\mathbf{x},t)$ can be determined by any method that is currently available (e.g., Brentner[20]). The term p'_Q accounts for all quadrupoles outside of the integration surface. In the current work, p'_Q is neglected.

The numerical solution to Eqns. (4-6) was implemented by Brentner and Farassat[17] in the code known as FW-H/RKIR. FW-H/RKIR is based upon a rotating Kirchhoff formulation for helicopter rotors developed by Lyrintzis and his colleagues.[21,22] For this work, the code was modified to remove helicopter blade motions. A preprocessor code was written to perform the task of interpolating the CFD data from CFL3D at each time step onto the integration surface used by FW-H/RKIR. The integration surfaces used here are not appropriate for Kirchhoff integration because they are located in the near field, rather than in the linear acoustic field. The preprocessor also replicated the two-dimensional (2D) surface data in the spanwise direction to simulate three-dimensional (3D) data. The integration surface used in the FW–H computations did not include the ends of the cylindrical integration surface. More information about the FW-H/RKIR code is provided by Brentner and Farassat.[17]

The Model Problems

The Cylinder

The first model problem consists of a circular cylinder in a cross flow. Brentner, Cox, Rumsey, and Younis[23] examined this general problem using similar computer codes. In their work, the integration surface for the FW–H code was chosen coincident with the physical surface. In our work, the integration surface is not restricted to the physical surface.

In this work a cylinder with a diameter D of 0.019 meters and span (of replicated two-dimensional data) that extends $40D$ (0.76 meters) is used. The free-stream Mach number is 0.2. Viscous two-dimensional calculations have been performed with a Reynolds number of 1000 based on free-stream velocity and cylinder diameter. The acoustic signal is observed at a position $128D$ (2.432 meters) from the cylinder center along a line mutually perpendicular to the free-stream direction and the cylinder axis. The CFD grid about the cylinder is stretched both radially and circumferentially such that more points are concentrated in the cylinder wake than

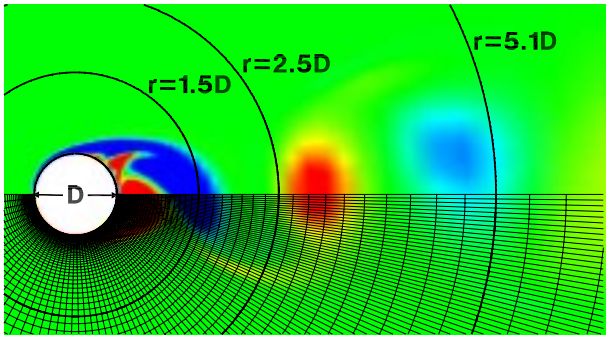

Figure 1. Vorticity field computed from CFD. FW–H integration surfaces are at $r = 0.5D$, $r = 1.5D$, $r = 2.5D$, and $r = 5.1D$

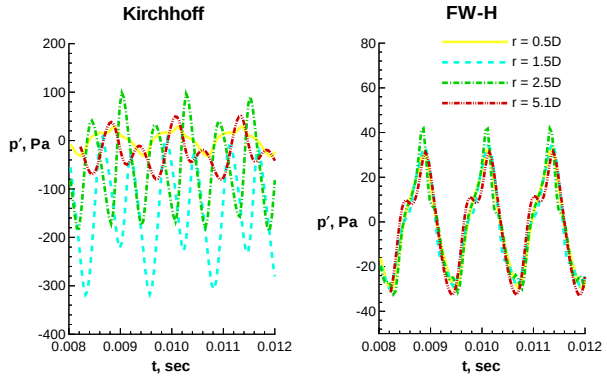

Figure 2. Acoustic signals computed for various integration surfaces that correspond to those indicated in Fig. 1.

upstream of the cylinder. FW–H integration surfaces have been taken on the cylinder surface ($0.5D$) and at radial distances from the cylinder axis of $1.5D$, $2.5D$, and $5.1D$. Fig. 1 renders an instantaneous vorticity field obtained from the CFD calculation with a superimposed grid distribution on the lower portion of the figure. The positions of the FW–H integration surfaces are indicated in the upper portion of the figure. Figure 2 shows the computed pressure signals at the observer for the different integration surfaces using a Kirchoff formulation and the FW–H formulation. The computed acoustic signal is not expected to vary with the integration surface location because Cox[24] has shown that the contribution of p'_Q is negligible. The use of an integration surface that cuts through the cylinder wake does not appear to adversely affect the results with the FW–H formulation. However, the figure shows that wildly varying results are obtained from a standard Kirchoff formulation for the same problem with the same integration surfaces.

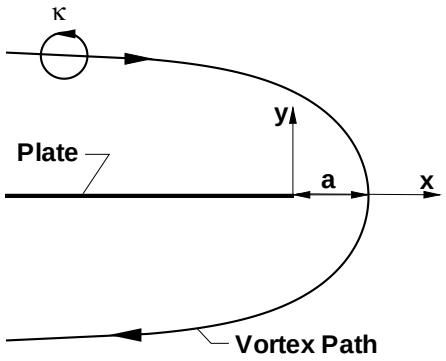

Figure 3. Line vortex moving around semi-infinite plate.

Line Vortex Around An Edge

The second model problem relates to the acoustic radiation from a 2D vortex filament moving around the edge of a half plane. This problem is solved analytically by Crighton[6] for low Mach numbers. Below we first summarize Crighton's analysis and then discuss the application of the FW–H acoustic code to the problem.

The incompressible motion of a line vortex around a rigid semi-infinite plate is determined by potential-flow theory. Figure 3 shows the salient features of the problem. A vortex of strength κ moves along the indicated path around the edge of the plate. The point of closest approach occurs at $x = a$, $y = 0$, at which time the vortex moves with speed $u = \kappa/4\pi a$. With the path of the vortex determined, the fluid is then assumed to be slightly compressible, that is, $M \equiv u/c << 1$. The spatial coordinates are rescaled by multiplication with the Mach number M and the limit taken as $M \to 0$. The velocity potential for the incompressible inner solution is matched to the velocity potential for the slightly compressible outer solution, and a radiation condition is applied to the outer solution at infinity. The resultant velocity potential, expressed in nondimensional form, is:

$$\phi(x, y, t) = \frac{4^{3/4}}{[(r-t)^2 + 4]^{1/4}} \frac{M^{1/2} \sin(\theta/2)}{r^{1/2}} \qquad (7)$$

where r is the nondimensional distance from the edge and θ is the angle measured relative to the positive x axis.

To test the ability of the FW–H acoustics code to propagate a scattered acoustic field, the exact acous-

tic solution to the problem, Eqn. 7, with $M = 0.01$ is used to establish flow conditions on an integration surface defined by a rectangular prism with $-200a \leq x \leq 2a$, $-2a \leq y \leq 2a$, $-500a \leq z \leq 500a$. Here z is the spanwise coordinate. On the $x = -200a$ face, the value of the pressure and wall-normal velocity at $y = 0$ is ambiguous because of a phase shift (between the upper and lower surfaces). Careful choice of integration points avoided the ambiguity. Later investigation revealed that the contributions to the acoustic signal from the $x = -200a$ face were so small that the entire $y - z$ face could be neglected without producing a noticeable change in the solution. Because of the low speed of the vortex compared with the speed of sound, the time required for the vortex to move from directly above the edge to directly below the edge is sufficient for an acoustic wave to travel $200a$. If that time span approximates the interaction time of the vortex with the edge, then we should expect a streamwise domain extent of at least $200a$ to be required. Figure 4 shows a comparison between the exact solution derived from Eqn. 7 and the numerically propagated solution for observers at a radius of $50a$ from the edge. To achieve these results, 250 cells are used to span the x direction, 50 cells are used to span the y direction, and 2500 cells are used to span the z direction. Numerical experimentation revealed a steady degradation of the results with reduction in the number of grid cells. Significant reduction in the domain extent in either the x or z direction also degrades the accuracy of the computed result. The results suggest that the FW–H integration surface must extend over a significant portion of the plate because the no-penetration boundary condition makes much of the plate appear to radiate. Hence the integration surface must extend to encompass all of these significant acoustic sources. The extensive integration domain required in the z direction is surprising. However, further analysis suggests that the oscillatory behavior of the integrand as a function of z results in the slow convergence to the 2D solution. In fact the difficulties with the z integration could be overcome by performing the z integration analytically using the method of stationary phase. Although such an option might be useful for this particular model problem, its extension to more complex problems is more difficult. In addition, our longer-term goal is to use the FW–H acoustics code for 3D problems, so performing the z integration numerically is more consistent with our expected future approach.

Because an exact incompressible solution is available for the vortex, this model problem also affords us the opportunity to explore conditions under which the incompressible solution could be used directly as input into the FW–H acoustics code. The integration surface for these tests is a surface displaced $10^{-5}a$ above and below the plate joined by a small circular region of radius $0.01a$ near the plate edge at $x = 0$. The computed solution displays a dipole-like directivity pattern centered on the plate edge, and not the cardioid shown in Fig. 4. For a noncompact source, as in this problem, these results show that the use of the incompressible solution to obtain integration surface quantities for use in a FW–H acoustics code leads to an incorrect solution if some method is not first introduced for accounting for a finite propagation time.

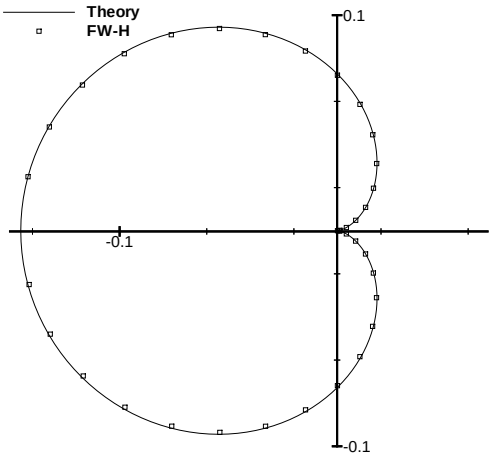

Figure 4. Acoustic pressure squared at $r = 50a$ for line vortex moving around semi-infinite plate with $M = 0.01$.

The Airfoil

We now address the edge noise problem by considering an airfoil with vortices convecting past its trailing edge. The calculations were performed using the inviscid option of CFL3D. The inviscid option was chosen to avoid having Reynolds number variations between runs with different Mach numbers. The small amount of numerically induced viscosity was expected to be sufficient to produce vortex roll-up shortly downstream of the vortex-generator plate, but otherwise not to interfere much with the flow past the airfoil trailing edge. The observed effects are discussed more fully below.

Geometry

In this model problem we have flow over a 2.6% thickness NACA 00 series airfoil. The cross section of the particular airfoil used is shown in Fig. 5(a).

The chord C is chosen to be 1 meter. For the purposes of the acoustic calculation, the span of the airfoil is twice the chord, or 2 meters. The thin airfoil enables a larger range of subsonic Mach numbers to be studied without the presence of transonic flow effects. Figure 5(b) shows a magnified view of the trailing edge of the airfoil. At 98% of the chord, a flat plate is introduced perpendicular to the flow. The flat plate extends from $0.0015C$ (1.5 mm) to $0.0025C$ (2.5 mm) above the airfoil chordline. In the presence of flow, vortices roll up just downstream of the flat plate, alternately near the plate's top and bottom edges. The chordwise location of the vortex-generator plate is a compromise between conflicting requirements. The plate needs to be sufficiently far from the trailing edge so that it does not interfere with the trailing edge scattering phenomenon. However, the realities of numerical dissipation and the need for extremely fine grid resolution to capture the shed vortices dictate that the distance from the vortex-generator plate to the trailing edge be minimized. The height of the plate $L = 1$mm ensures that the acoustic wavelength λ of the dominant frequency scattered by the trailing edge is much smaller than the chord (i.e., $\lambda/C << 1$). The dominant shedding frequency f_s is related to the plate height via the Strouhal number $St = Lf_s/U_0$ where U_0 is the free-stream velocity. The dominant acoustic frequency is expected to equal the vortex shedding frequency. By expressing the acoustic wavelength in terms of f_s and the sound speed c, we can relate λ/C to the Strouhal number, the Mach number $M_0 = U_0/c$, and the normalized flat plate height L/C by

$$\lambda/C = \frac{L/C}{St \cdot M_0} \tag{8}$$

With an estimated Strouhal number between 0.1 and 0.2 and a free-stream Mach number of 0.2, the chosen $L/C = 0.001$ satisfies the constraint $\lambda/C << 1$ even with moderate variations in the Strouhal number and the Mach number.

CFD grid

The CFD grid requirements are driven by the unsteady flow. Extremely fine gridding is required downstream of the vortex-generator plate to guarantee that the complex physics associated with the vortex dynamics leading to acoustic scattering at the edge is resolved. Because the flow is noncompact, the grid needs to resolve the dominant acoustic waves radiated over the surface of the airfoil. Far from the airfoil, the only important requirement is that no reflections from boundaries interfere with the calculation. To meet these requirements, we implemented a 7-zone patched grid. Each zone contains a stretched and sometimes slightly skewed Cartesian mesh. The use of Cartesian meshes with patched interfaces at the zone boundaries make grid modifications particularly easy. The finest grid used had the zonal grid resolutions as indicated in Fig. 6. Figure 7 shows a magnified view of the grid in the vicinity of the bluff body. For clarity, only every fourth grid line is shown in Fig. 7. The computational domain extends $2C$ upstream of the leading edge, $2C$ downstream of the trailing edge, and $2C$ above and below the airfoil chordline. The grid downstream of the trailing edge is stretched sufficiently to diffuse the vortices long before they encounter the computational domain outflow boundary.

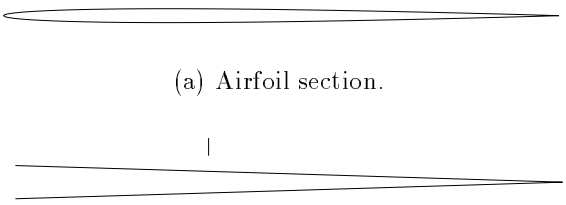

(a) Airfoil section.

(b) Magnified view of trailing edge and vortex-generator plate.

Figure 5. View of geometry.

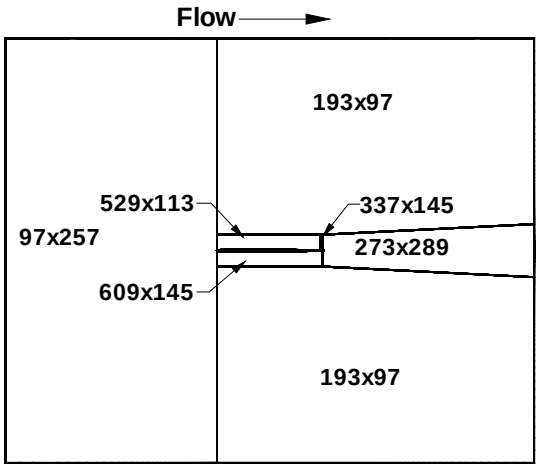

Figure 6. Resolution in 7-zone grid.

At the upstream boundary, free-stream conditions are imposed. Above and below the airfoil, far-field conditions for the normal velocity and the speed of sound are obtained from two locally one-dimensional Riemann invariants. The downstream outflow boundary employs simple extrapolation.

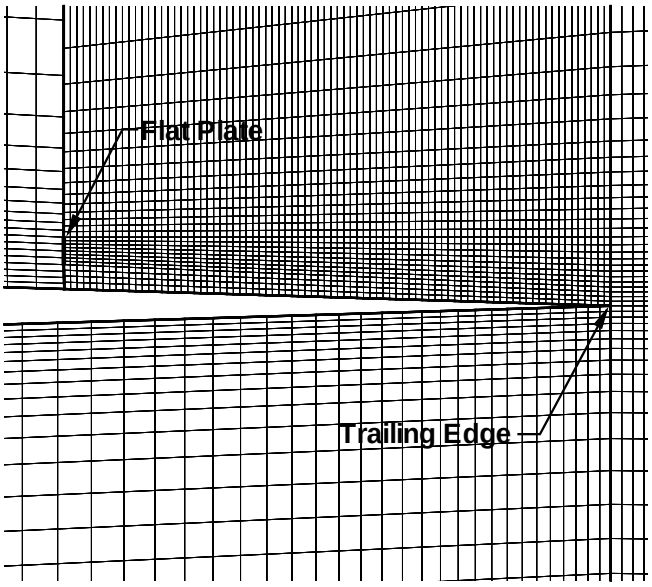

Figure 7. Magnified view of grid in vicinity of bluff body. Actual flat plate has zero thickness. Every fourth grid line is shown.

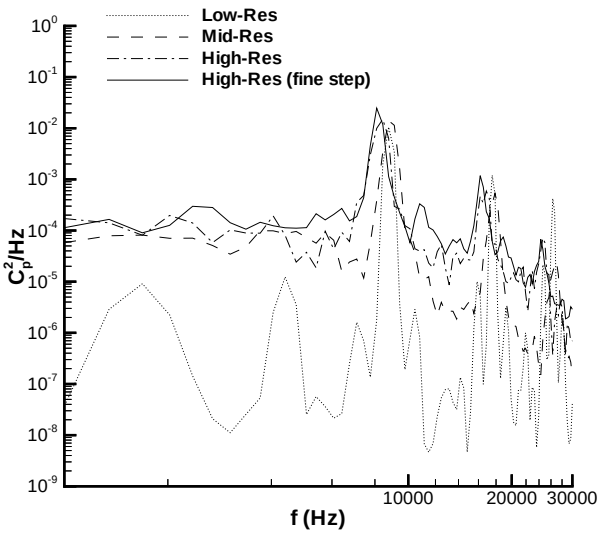

Figure 8. Spectra of pressure coefficient under vortex-generator plate for different grid resolutions. $M = 0.2$.

The calculations are performed on two coarser grids, each successively halving the grid resolution in each direction. The two coarser grids are run with a time step of $0.001C/c$. Three cases with the finest grid were run with the time step varying from $0.001C/c$ to $0.00025C/c$.

Effects of varying grid resolution

Some important changes in the overall flow features occur as the CFD grid resolution and time step are varied. As an indication of these changes, Fig. 8 shows the spectra of the pressure coefficient for the different resolutions at a location directly under the vortex-generator plate. At the lowest resolution, the spectrum is dominated by the peaks at the shedding frequency and its harmonic. Increasing the grid resolution fills the spectrum more fully and shifts the shedding frequency slightly lower. Similarly, the spectrum becomes fuller and the dominant frequency shifts slightly lower as the time step is decreased. Observations of the time-dependent flow data revealed that both increased grid resolution and a finer time step results in more vortex amalgamation in the region between the vortex-generator plate and the airfoil trailing edge.

In hindsight, the variation of the results with grid resolution and time step should have been expected. Originally, an inviscid calculation was chosen in order to avoid Reynolds-number variations for runs with different Mach numbers. With no physical viscosity in the calculations, dispersion and dissipation are governed by the numerical truncation error, which is expected to be small in the region between the vortex generator plate and the airfoil trailing edge. Unfortunately, the process of vortex amalgamation is sensitive to the physical viscosity. Hence, in the numerically simulated cases, even small differences in the numerically introduced effective viscosity produces noticeable changes in the results. Results at different Mach numbers are therefore also at different effective Reynolds numbers, the very effect that we originally sought to avoid. In part because of these difficulties, the results obtained are useful in that they provide guidance as to the problems and capabilities of the hybrid calculation procedure for complex flows. In future work, the effects of including viscosity and turbulence modeling should be investigated.

In what follows, all results have been obtained using the highest resolution grid with the smallest time step.

General flow features

Figure 9 shows vorticity magnitude contours in the vicinity of the trailing edge at a single time step. The circular concentrations of vorticity indicate the individual vortices that comprise the unsteady Karman vortex street downstream of the vortex-generator plate. Vortices are shed alternately from opposite ends of the vortex-generator plate. At a Mach number of 0.2, the Strouhal number of the

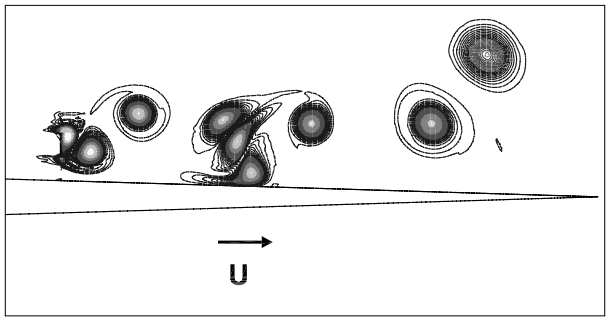

Figure 9. Instantaneous vorticity magnitude contours in vicinity of trailing edge for $M = 0.2$ case. Approximately 2% of aft portion of airfoil is shown.

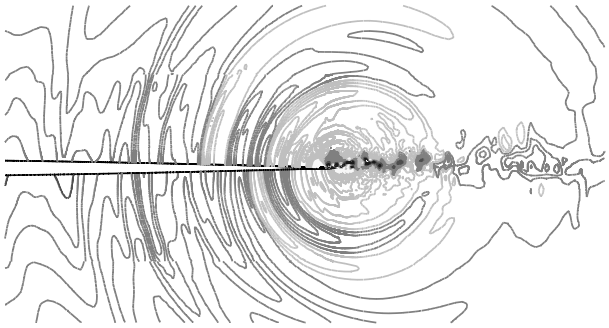

Figure 10. Instantaneous pressure contours (with restricted min-max limits) over approximately 40% of aft portion of airfoil for $M = 0.2$ case.

vortex shedding is approximately 0.12 based upon the height of the flat-plate vortex generator and the free-stream speed. At a Mach number of 0.4, the Strouhal number of the vortex shedding is approximately 0.13. If the Strouhal number were based on the actual convection speed of the vortices, the Strouhal number would be somewhat larger. The frequency of the vortices convecting past the trailing edge is less distinct because the vortices shed from the vortex-generator plate often pair and interact with neighboring vortices as seen in Fig. 9.

Figure 10 shows instantaneous pressure contours in the vicinity of the trailing edge of the airfoil. The contours have been restricted to a narrow range about the mean pressure so that the acoustic waves emanating from the trailing edge are more visible. The figure clearly shows the upstream propagation of acoustic waves that results from the vortices passing close to the airfoil trailing edge.

Acoustics

The FW–H code computes the acoustic field generated by the unsteady aerodynamic flow field. In this work we explore the use of two different integration surfaces, one on the airfoil body and a second surface approximately 1% of the chord off the airfoil. Figure 11(a) shows the off-airfoil-body integration surface together with the airfoil body. Figure 11(b) shows a closeup of the trailing-edge area. The region enclosed by the off-airfoil-body surface includes all of the vortices between the bluff body and trailing edge as well as the first few vortices in the wake region. We observe that the resolution of the integration surface is least critical (for numerical reasons) when a straight line is used to close the downstream end of the surface. Our tests indicate that increasing the number of points on the integration surface (via interpolation of the CFD data) results in only small changes in the observed acoustic signals.

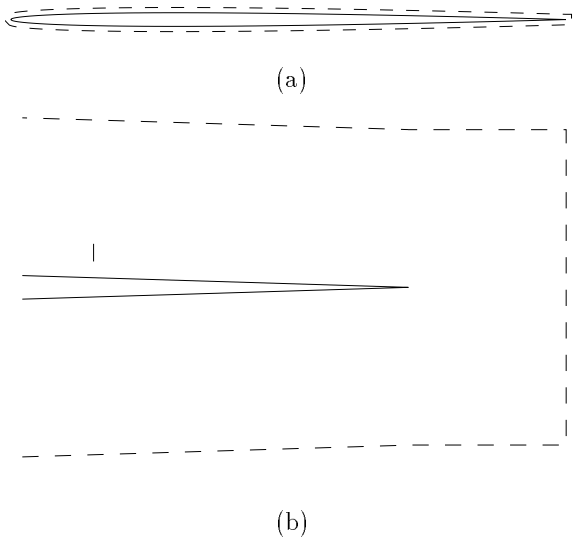

Figure 11. Integration surfaces used for acoustics calculations. Short vertical line indicates location of vortex-generator plate. ——— On-airfoil-body integration surface; – – – – – Off-airfoil-body integration surface.

The far-field signals are obtained at several observer locations. For the data shown here, the observers are all located $10C$ (10 meters) from the trailing edge of the airfoil. Figure 12 shows spectra of the acoustic signal for several observer positions. The angular measurements are increasingly positive for counterclockwise rotations with 0 degrees being directed downstream. The figure shows much reduced noise radiation directly upstream and directly downstream.

Integration of the acoustic spectrum over the frequencies provides the mean square acoustic pressure. Variation of the mean square acoustic pressure as a function of Mach number is plotted in Fig. 13. The

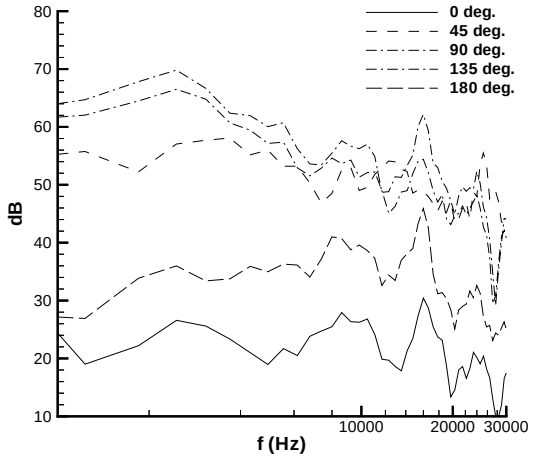

Figure 12. Spectra of acoustic signals (referenced to 20μPa) for various observers all located $10C$ from trailing edge of airfoil. On-airfoil-body integration surface used, $M = 0.2$.

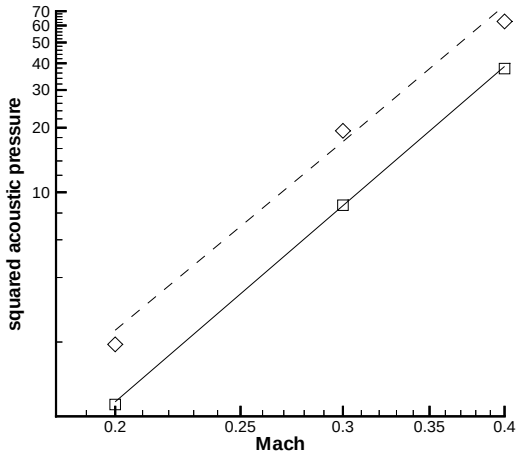

Figure 13. Variation in mean-square acoustic pressure versus Mach number. ▫ data for 30 degs.; ——— least-squares fit for 30 degs.; ◇ data for 45 degs.; – – – – – least-squares fit for 45 degs.

symbols show the data, and the lines are a linear least-squares fit to the logarithm of the data. For an observer at 30 degrees, the mean square pressure varies as the 5.2 power of Mach number. For an observer at 45 degrees, the data do not align quite so well, but least-squares regression indicates variation with the 5.0 power of Mach number. Theoretically, we expect the scaling law to be M^4 for the 2D case of vortices convecting past the edge of a semi-infinite rigid plate and we assume a similar result will occur for the airfoil of finite chord, as used in our problem. Currently we do not possess a general theory for the airfoil of finite chord. This scaling would be obtained by assuming complete coherence in the spanwise direction and integrating the result of Ffowcs Williams and Hall[3] for infinitesimal Mach numbers along the infinite span. In addition to the finite Mach numbers used in the CFD (as opposed to the infinitesimal Mach number of the theory), another source of the discrepancy between the theoretical M^4 scaling law and the value of $M^{5.2}$ obtained from the computations is that the root mean square (rms) fluctuating velocity above the airfoil does not vary linearly with free-stream velocity, but instead varies as $M^{1.34}$. Accounting for the actual rms fluctuating velocity, a scaling of $M^{5.36}$ is implied, which is in close agreement with our computationally observed scaling of $M^{5.2}$. We note that this close agreement has only been obtained by neglecting the Doppler corrections as predicted by Howe[7] for the semi-infinite flat plate. Our data do not appear to support the effect of significant Doppler correction terms, at least up to $M = 0.4$.

The directivity of the acoustic signals is shown in Figs. 14a and b. To show the results for all three Mach numbers on the same plot the mean square pressures are scaled with $M^{-5.2}$. Figure 14a, shows the case in which the integration surface is on the airfoil body. The null regions in the vicinity of 0 degrees and 180 degrees are typical of acoustic scattering over a finite streamlined body (c.f. Fig. 3.14 of Wagner, Bareiss, and Guidati[9]). Note that the scaling collapses the results for the different Mach numbers reasonably well. Figure 14b shows the results for cases in which the off-airfoil-body integration surface is used. The data still collapse satisfactorily in the region under the airfoil, but not so well above the airfoil. The upper-lower asymmetry in Fig. 14b suggests that the shedding of the vortices from the vortex-generator plate produces noise that radiates predominantly above the airfoil. The noise produced by the vortex-generator plate is not included in any of the edge-scattering theories. The noise that radiates below the airfoil is likely to be dominated by the field scattered by the trailing edge.

In Fig. 15, we compare the directivity of the acoustic signal to the $\sin^2(\theta/2)$ directivity for an acoustic source near the edge of a rigid half-plane. The amplitude of the $\sin^2(\theta/2)$ prediction is matched with the amplitude of the computed acoustic signal at 30 degrees. All of the acoustic signals in Figs. 15 are computed using the on-airfoil-body integration

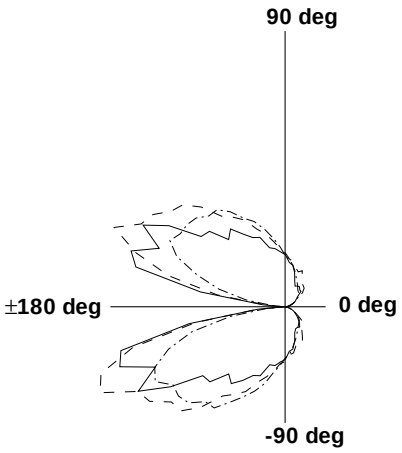

(a) On-airfoil-body integration surface.

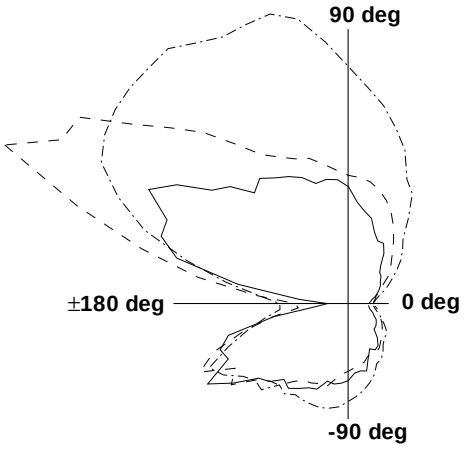

(b) Off-airfoil-body integration surface.

Figure 14. Scaled directivity of squared pressure for observers 10 chord lengths from trailing edge. Squared pressure is scaled with $M^{-5.2}$. Both (a) and (b) use same scale. ——— $M = 0.2$; – – – – – $M = 0.3$; –·–·–·– $M = 0.4$.

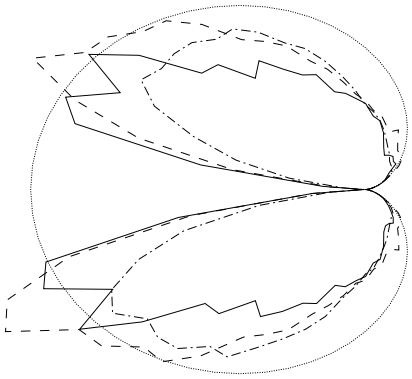

Figure 15. Scaled squared pressure with cardioid included. Squared pressure is scaled with $M^{-5.2}$. ——— $M = 0.2$; – – – – – $M = 0.3$; –·–·–·– $M = 0.4$; ····· cardioid.

surface. For all three Mach numbers, the agreement with the theoretically predicted pattern is very good for $-45^o < \theta < 45^o$. Beyond that range the effects of the diffraction from the leading-edge and the coarser grid resolution on the middle and upstream portions of the airfoil affect the computed directivity.

Conclusions

Three model problems were investigated to address the fitness of the hybrid CFD/FW–H method for predicting acoustics in complex flow fields.

The first model problem involved the sound generated by vortex shedding from a circular cylinder with axis normal to the flow. We showed that the FW–H approach provides consistent acoustic signals for integration surfaces both on and off the body, even when the off-airfoil-body integration surfaces intersected the cylinder wake. In contrast, a Kirchhoff formulation that uses the same integration surfaces gives erratic results with acoustic signals varying by more than an order of magnitude.

The second model problem sought to confirm the ability of the FW–H approach to correctly predict the acoustic propagation associated with edge scattering. We chose to study Crighton's[6] exact model problem of a line vortex traveling around the edge of a rigid half plane under its own induced velocity field. We found that the FW–H approach correctly predicts the far field noise provided that the integration surface extends sufficiently far upstream and laterally. The upstream extent should be far enough to include the passage of acoustic waves that are

produced during the time that the vortex is in the vicinity of the half-plane edge. The spanwise extent needs to be long enough to converge a slowly varying oscillatory integral, which results from attempting to compute a strictly 2D case in a 3D acoustic computation. As an aside, we found that the incompressible results cannot be used directly to provide unsteady flow data on the integration surface for cases in which the acoustic source is not compact.

Finally, we investigated using CFD to simulate the flow of vortices convecting past the trailing edge of an airfoil and the FW–H approach to obtain the noise produced. Because vortex generation and vortex interaction are inherently viscous phenomena, the small amount of artificial viscosity of the inviscid CFD alters the character of the flowfield with grid resolution. In spite of this, many of the expected acoustic features of the flow are observed when the time-accurate CFD data are used as input for a FW–H analysis. The general directivity pattern is similar to that illustrated in Wagner, Bareiss, and Guidati.[9] In fact, the half-plane prediction of a $\sin^2(\theta/2)$ dependency of the intensity is observed in the quadrant around the trailing edge. Velocity scaling of the computed acoustic signal suggests an approximate $M^{5.2}$ dependency although extension of the Ffowcs Williams and Hall[3] analysis for $M \to 0$ to 2D configurations implies a M^4 dependency. Accounting for the nonlinear dependence of the rms velocities at the trailing edge with free-stream Mach number improves the agreement between the calculations and the theoretical predictions. Without a complete theory that includes the finite chord of the airfoil and the finite Mach numbers of the flows, the current agreement is as good as we should expect.

Acknowledgments

The authors thank Drs. Christopher Rumsey and Robert Biedron for many useful suggestions in the use of CFL3D.

References

1. Lighthill, M. J., "On Sound Generated Aerodynamically, I: General Theory," *Proceedings of the Royal Society*, Vol. A221, 1952, pp. 564–587.

2. Lighthill, M. J., "On Sound Generated Aerodynamically, II: Turbulence as a Source of Sound," *Proceedings of the Royal Society*, Vol. A222, 1954, pp. 1–32.

3. Ffowcs Williams, J. E., and Hall, L. H., "Aerodynamic Sound Generation by Turbulent Flow in the Vicinity of a Scattering Half Plane," *Journal of Fluid Mechanics*, Vol. 40, 1970, pp. 657–670.

4. Curle, N., "The Influence of Solid Boundaries upon Aerodynamic Sound," *Proceedings of the Royal Society*, Vol. 231, 1955, pp. 505–514.

5. Goldstein, M. E., *Aeroacoustics*, McGraw-Hill Book Company, 1976.

6. Crighton, D. G., "Radiation from Vortex Filament Motion Near a Half-Plane," *Journal of Fluid Mechanics*, Vol. 51, No. 2, 1972, pp. 357–362.

7. Howe, M. S., "A Review of the Theory of Trailing Edge Noise," *Journal of Sound and Vibration*, Vol. 61, No. 3, 1978, pp. 437–465.

8. Brooks, T. F., and Hodgson, T. H., "Trailing Edge Noise Prediction from Measured Surface Pressures," *Journal of Sound and Vibration*, Vol. 78, No. 1, 1981, pp. 69–117.

9. Wagner, S., Bareiss, R., and Guidati, G., *Wind Turbine Noise*, Springer, 1996.

10. Ffowcs Williams, J. E., and Hawkings, D. L., "Sound Generated by Turbulence and Surfaces in Arbitrary Motion," *Philosophical Transactions of the Royal Society*, Vol. A264, No. 1151, 1969, pp. 321–342.

11. Rumsey, C., Biedron, R., and Thomas, J., "CFL3D: Its History and Some Recent Applications," TM 112861, NASA, May 1997. presented at the Godonov's Method for Gas Dynamics Symposium, Ann Arbor, MI.

12. Krist, S. L., Biedron, R. T., and Rumsey, C., *CFL3D User's Manual*, Aerodynamic and Acoustic Methods Branch, NASA Langley Research Center, 1997. Version 5.

13. Roe, P., "Approximate Riemann Solvers, Parameter Vectors and Difference Schemes," *Journal of Computational Physics*, Vol. 43, 1981, pp. 357–372.

14. Biedron, R. T., and Thomas, J. L., "A Generalized Patched-Grid Algorithm with Application to the F-18 Forebody with Actuated Control Strake," *Computing Systems in Engineering*, Vol. 1, No. 2-4, 1990, pp. 563–576.

15. Rumsey, C. L., Sanetrik, M. D., Biedron, R. T., Melson, N. D., and Parlette, E. B., "Efficiency and Accuracy of Time-Accurate Turbulent Navier-Stokes Computations," *Computers and Fluids*, Vol. 25, No. 2, 1996, pp. 217–236.

16. Rumsey, C. L., Biedron, R., Farassat, F., and Spence, P. L., "Ducted-Fan Engine Acoustic Predictions Using A Navier-Stokes Code," *Journal of Sound and Vibration*, Vol. 213, No. 4, 1998, pp. 643–664.

17. Brentner, K. S., and Farassat, F., "An Analytical Comparison of the Acoustic Analogy and Kirchoff Formulation for Moving Surfaces," *AIAA Journal*, Vol. 36, No. 8, 1998, pp. 1379–1386.

18. Farassat, F., and Succi, G. P., "The Prediction of Helicopter Discrete Frequency Noise," *Vertica*, Vol. 7, No. 4, 19883, pp. 309–320.

19. Brenter, K. S., *Prediction of Helicopter Discret Frequency Rotor Noise – A Computer Program Incorporating Realistic Blade Motions and Advanced Formulation*, NASA Langley Research Center, Oct 1986. TM 87721.

20. Brentner, K. S., "An Efficient and Robust Method for Predicting Helicopter Rotor High-Speed Impulsive Noise," *Journal of Sound and Vibration*, Vol. 203, No. 1, 1997, pp. 87–100.

21. Xue, Y., and Lyrintzis, A. S., "Rotating Kirchhoff Method for Three-Dimensional Transonic Blade-Vortex Interaction Hover Noise," *AIAA Journal*, Vol. 32, No. 7, July 1994, pp. 1350–1359.

22. Lyrintzis, A. S., Koutsavdis, E. K., Berezin, C., Visintainer, J., and Pollack, M., "Kirchoff Acoustic Methodology Validation and Implementation in the TiltRotor Aeroacoustic Codes (TRAC)," American Helicopter Society 2nd International Aeromechanics Specialists' Conference, Oct 1995.

23. Brentner, K. S., Cox, J. S., Rumsey, C. L., and Younis, B. A., "Computation of Sound Generated by Flow Over a Circular Cylinder: An Acoustic Analogy Approach," *Second Computational Aeroacoustics (CAA) Workshop on Benchmark Problems*. NASA, 1997, pp. 289–296. NASA Conference Publication 3352.

24. Cox, J. S., "Computation of Vortex Shedding and Radiated Sound for a Circular Cylinder: Subcritical to Transcritical Reynolds Numbers," Master's thesis, The George Washington University, Aug 1997.